frontiers in Materials

ORIGINAL RESEARCH
published: 28 August 2020
doi: 10.3389/fmats.2020.00228

The Effect of Cold Swaging Deformation on the Microstructures and Mechanical Properties of a Novel Metastable β Type Ti–10Mo–6Zr–4Sn–3Nb Alloy for Biomedical Devices

Jun Cheng[1,2], Hongchuan Wang[3], Jinshan Li[1], Jinyang Gai[4], Jinming Ru[5], Zhaoxin Du[6], Jiangkun Fan[1], Jinlong Niu[2], Hongjie Song[2] and Zhentao Yu[7]*

[1] State Key Laboratory of Solidification Processing, Northwestern Polytechnical University, Xi'an, China, [2] Northwest Institute for Nonferrous Metal Research, Shaanxi Key Laboratory of Biomedical Metal Materials, Xi'an, China, [3] School of Material Science and Engineering, Northeastern University, Shenyang, China, [4] State Key Laboratory of Powder Metallurgy, Central South University, Changsha, China, [5] Institute for Advanced Manufacturing and Modern Equipment Technology, Jiangsu University, Zhenjiang, China, [6] School of Materials Science and Engineering, Inner Mongolia University of Technology, Hohhot, China, [7] Institute of Advanced Wear and Corrosion Resistant and Functional Materials, Jinan University, Guangzhou, China

OPEN ACCESS

Edited by:
Liang-Yu Chen, Jiangsu University of Science and Technology, China

Reviewed by:
Liqiang Wang, Shanghai Jiao Tong University, China
Lechun Xie, Wuhan University of Technology, China

***Correspondence:**
Jun Cheng
524161386@qq.com

Specialty section:
This article was submitted to Structural Materials, a section of the journal Frontiers in Materials

Received: *26 May 2020*
Accepted: *22 June 2020*
Published: *28 August 2020*

Citation:
Cheng J, Wang H, Li J, Gai J, Ru J, Du Z, Fan J, Niu J, Song H and Yu Z (2020) The Effect of Cold Swaging Deformation on the Microstructures and Mechanical Properties of a Novel Metastable β Type Ti–10Mo–6Zr–4Sn–3Nb Alloy for Biomedical Devices. Front. Mater. 7:228. doi: 10.3389/fmats.2020.00228

This work investigated the microstructures, texture evolution, and mechanical properties of newly designed metastable β type Ti–10Mo–6Zr–4Sn–3Nb (wt.%) alloys for biomedical devices, which were subjected to cold swaging deformation with reductions of 15–75%. With the increment in the reduction of swaging deformation, the grains are broken and gradually refined, and stress-induced martensite transformation takes place, resulting in the formation of the α" phase. Moreover, the {1 1 2} <1 1 1> and {1 1 0} <1 1 2> fibers turn into γ-fiber {1 1 1} <1 1 0> and α-fiber {1 1 2} <1 1 0> with the increment in the swaging reduction. The α-fiber texture in particular, first weakens and then strengthens during cold deformation. Under the combined effect of sub-structures, grain refinement, and texture evolution, the strength of the alloy is gradually enhanced with the increment in the cold deformation reduction. The solution-treated alloy bar shows superior cold workability in the swaging process. The plasticity remains at a moderate level because the initial grains have not been completely broken at the beginning of cold swaging deformation. The elastic modulus of the alloy shows a downward trend with an increasing reduction, which is related to the dislocation multiplication, grain refinement, and grain orientation evolution during cold swaging deformation.

Keywords: Ti–10Mo–6Zr–4Sn–3Nb alloy, cold swaging deformation, microstructure, mechanical properties, texture evolution, metastable β Ti alloy

INTRODUCTION

Titanium alloys are significantly promising biomedical metallic materials applied in dental and orthopedic implants due to higher specific strength, excellent corrosion resistance, superior biocompatibility, and outstanding comprehensive mechanical properties (Niinomi, 2008; Geetha et al., 2009; Niinomi et al., 2012; Gepreel and Niinomi, 2013; Ramezannejad et al., 2019; Zhang and Chen, 2019). In recent years, biological safety to patients has become crucial in biomedical metallic materials (Li and Zheng, 2016; Ibrahim et al., 2017; Zhang et al., 2020). In the human body, a small number of released metal ions, such as V, Al, and Ni, may induce an allergic response and carcinogenesis (Chen and Thouas, 2015). Therefore, β titanium alloys with no toxic elements are considered to be ideal candidates and have been used for surgical implants (Eisenbarth et al., 2004). In addition, as a replacement for failed hard tissue, the high strength and low elasticity modulus of β Ti alloy are considered as a desired biomechanical advantage, owing to the decrease in the risk of stress shielding and bone fracturing (Hao et al., 2012; Bahl et al., 2018; Li et al., 2019). For instance, Ti–24Nb–4Zr–8Sn and Ti–25Nb–3Zr–2Sn–3Mo, two representative novel metastable β type titanium alloys for orthopedic applications were developed based on the Bo–Md diagram (Hao et al., 2007; Zhan et al., 2016). The stability of the β phase is improved by addition of Mo, Zr, Sn, and Nb alloying elements, and the β phase with body-centered cubic structures can also be maintained in the alloy after being solution-treated above the β transus temperature (Cai et al., 2013; Zhang et al., 2017). The elastic modulus can be reduced by addition of Nb and Zr, while the precipitation of the hard and brittle phase (such as ω phase) can also be hindered by addition of Sn and Zr. Despite the importance of alloying elements, a problem remain in that the Young's modulus for the alloy still exceeds that for the bone tissue (10–30 GPa).

Previous studies reported that the low elastic modulus of titanium and its alloys could be obtained by cold deformation (Plaine et al., 2019). The deformation textures, dislocations slipping or tangles, and other crystalline defects generated in the cold deformation process have a large influence on the strength-ductility balance of titanium and its alloys (Lan et al., 2017; Rabadia et al., 2019a,b; Liang et al., 2020). Furthermore, the elastic moduli of titanium and its alloys also change with the type and intensity of the texture. In order to obtain good biomechanical compatibility, an alloy with a lower elastic modulus and an acceptable strength is expected (Meng et al., 2014; Callioglu and Acar, 2020). Wang et al. (2008) reported that the modulus of the Ti–35Nb–2Ta–3Zr alloy decreased gradually with the increase in cold rolling reduction due to the appearance of stress-induced α" martensite plates. Xu et al. (2012) investigated the influence of cold rolling deformation on the microstructures, texture evolution, phase transformation, deformation mechanisms, and mechanical properties for a novel β type Ti–25Nb–10Ta–1Zr–0.2Fe alloy; they found that the intensity of α-fiber texture reduces and the γ-fiber texture gradually changes to the primary component at a 60% reduction; for the γ-fiber textures, {1 1 1} <1 1 0> texture weakens and gradually changes to the {1 1 1} <1 1 2> component.

The Ti–10Mo–6Zr–4Sn–3Nb alloy developed by NIN (Northwest Institute for Non-ferrous Metal Research, Xi'an, China) is a novel meta-stable β titanium alloy for potential orthopedic application due to its non-toxicity, low modulus, and moderate strength. In addition, cold swaging deformation is a three-dimensional compressive stress processing method, which is similar to rolling (Mori et al., 2016). The advantages of this method are the easy replacement of forging die, a smooth surface, and a high dimensional accuracy. To date, however, few studies have focused on the cold deformation mechanisms, microstructure/texture evolution, and mechanical properties of the Ti–10Mo–6Zr–4Sn–3Nb alloy.

In this work, the cold swaging deformation of the Ti–10Mo–6Zr–4Sn–3Nb alloy bars was carried out with reductions of 15–75%. This work aims to clarify the influence of cold swaging deformation on the microstructural characteristic, texture evolution, deformation mechanisms, and mechanical properties of a novel metastable β type Ti–10Mo–6Zr–4Sn–3Nb alloy. It is expected that the superior combination of a low elastic modulus and a high strength can be obtained using an appropriate deformation method for surgical implant applications.

EXPERIMENTAL PROCEDURE

The raw materials used for the Ti–10Mo–6Zr–4Sn–3Nb alloy consist of a titanium sponge, zirconium sponge, Ti–32Mo, Ti–60Sn, and a Nb–47Ti master alloy. The ingot was prepared using vacuum arc remelting (VAR) three times in order to avoid alloy segregation and to ensure uniformity. The chemical compositions of investigated alloys are listed in **Table 1**. To obtain a fine and uniform microstructure, multiple forging at 1030°C (β phase region) refined the as-cast microstructure which has coarse grains. The alloy bars with 10 mm were hot rolled at around 850°C. The last processing step was to straighten and ground the bar to improve the product surface quality. The β transus for the Ti–10Mo–6Zr–4Sn–3Nb alloy was measured as being approximately 760°C using metallographic observations. The bars were divided into many pieces to conduct heat treatments and a swaging experiment. The specimens were first solution annealed at 790°C for 1 h and water quenched to retain a single β phase at room temperature. The cold swaging was carried out with reductions of 15, 25, 35, 45, 55, 65, and 75%, respectively. Both the solution treatments and swaging deformation were performed in the atmosphere. The oxidation layer of the sample was removed using the NC machine tool.

The surface of the sample was ground and polished with 400, 600, 800, 1000, and 2000 # abrasive paper and a diamond paste. The polished specimens were etched in Keller's solution (10% HF, 20% HNO_3, and 70% H_2O in vol.%) to reveal the microstructure at various conditions. All of the metallographic microstructure

TABLE 1 | Chemical compositions of the Ti–10Mo–6Zr–4Sn–3Nb alloy (wt%).

Ti	Mo	Zr	Sn	Nb	C	N	O	H
Bal.	10.11	5.71	4.32	2.83	0.024	0.017	0.11	0.0037

observations were conducted using the OLYMPUS PMG3 optical microscope (OM). The phase composition was determined by X-ray diffraction (XRD) with BRUKER D8 ADVANCE, using copper K_α radiation at a voltage of 40 kV and a current of 40 mA. The result analysis was conducted with a 2-theta angle ranging from 30 to 90° and with a constant step size of 0.02°. The preparation of transmission electron microscopy (TEM) samples was performed using the twin jet polishing method in a solution of 6% perchloric, 35% methanol, and 59% butanol (vol%) at −30°C. The TEM characterization was carried out using a FEI TECNAI G2 F20 instrument operated at a voltage of 300 kV. The electron backscattered diffraction (EBSD) analysis was conducted using FEI Quanta 650F plus HKL Channel 5 software to investigate the texture evolution with orientation distribution functions (ODFs). The samples for EBSD measurement were prepared by a vibratory polisher (Buehler) using a kind of oxide polishing liquor for 9 h, in order to eliminate the surface residual stress. The tensile testing was performed at room temperature using an INSTRON testing instrument with 0.005 mm min^{-1}. Samples were machined for the tensile tests according to the ASTM E8/E8M standard. The diameter and gage length of each sample were 6and 25 mm, respectively.

RESULTS AND DISCUSSION

The Influence of Swaging Deformation on Microstructure

The XRD patterns of the Ti–10Mo–6Zr–4Sn–3Nb alloy samples, with the conditions of solution-treated at 790°C/1 h, water quenching (WQ), and cold swaging with reductions of 15, 25, 35, 45, 55, 65, and 75% are displayed in **Figure 1**. As seen in the **Figure 1A**, the diffraction peaks of (1 1 0), (2 0 0), (2 1 1), and (2 2 0) that correspond to the β phase are apparent. The diffraction peaks of the β phase still exist after cold deformation at various reductions. To the author's knowledge, the phase transformation of β→α" could take place during the cold deformation (Qi et al., 2019). Unfortunately, the diffraction peaks corresponding to the α" phase were not detected. When the content of the detected α" phase is less than 5%, it cannot be detected by XRD (Banerjee and Williams, 2013). However, it can be observed and characterized by a transmission electron microscope in a micro area. With the increment in the reduction of swaging deformation, the intensities of diffraction peaks of (2 0 0) and (2 1 1) tend to weaken and finally disappear. It can be inferred that the crystallographic orientations of <2 0 0> and <2 1 1> reduce after cold swaging deformation. In contrast, with the increment in the reduction, the diffraction intensity of the (2 2 0) peak first decreases and then increases. In XRD patterns, the full width half maximum (FWHM) of diffraction peaks for deformed metallic materials is used to assess the crystal lattice distortion, owing to the appearance of a dislocation or a crystal cell distortion (Xu et al., 2016). As seen in **Figure 1B**, it can be observed that the FWHM of the (1 1 0) peak first increases up to reduction of 55% and subsequently decreases after a reduction of 75%. The reason is that a large number of dislocations are produced during cold swaging deformation. The stress concentration results from dislocation tangles on the various slip systems (combinations of slip plane and slip direction). Furthermore, the lattice distortion resulted from the increment in the interior stress results in the decrease in the grain size as well as the increase in the density of dislocations, sub-grains, and sub-boundaries during the cold swaging deformation. Due to the inhomogeneous cold swaging deformation, the external region is more severe than the internal counterpart during deformation. With the increase in the cold deformation reduction, the inhomogeneous deformation would be alleviated. It can be seen from microstructural evolution that most grains gradually turn into fibrous after deformation at a 55% reduction. Moreover, the reason for the decrease in the FWHM value in the

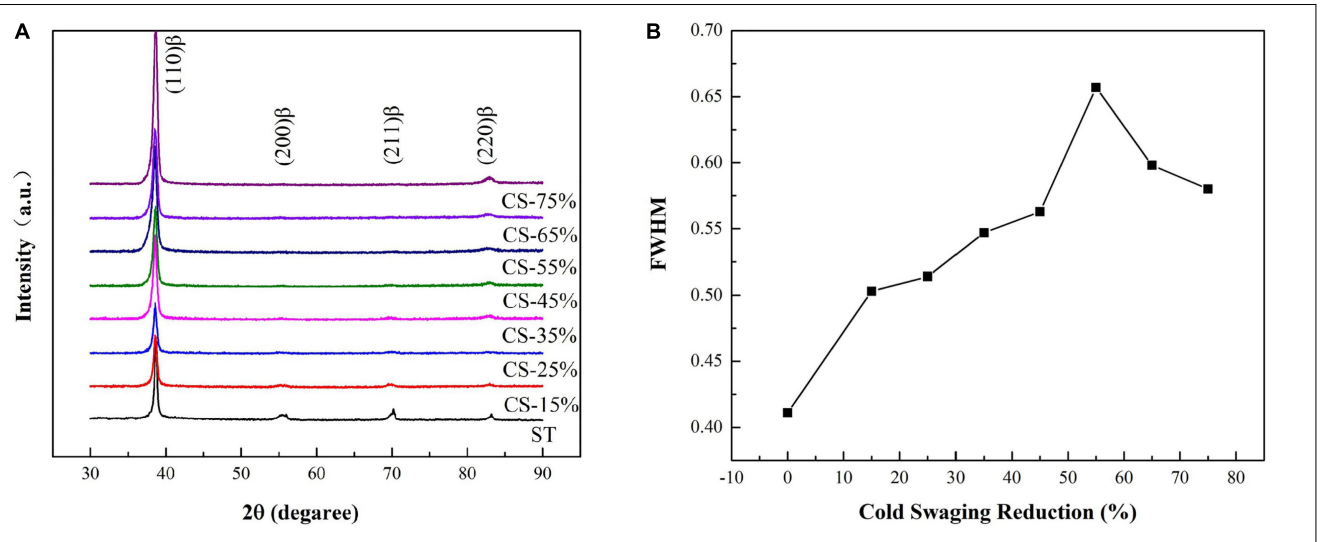

FIGURE 1 | (A) XRD profiles of the Ti-10Mo-6Zr-4Sn-3Nb alloy solution annealed at 790°C/1 h, water quenching and cold deformed with reductions of 15, 25, 35, 45, 55, 65, and 75%; **(B)** The relationship between cold swaging reduction and full width half maximum (FWHM) of (1 1 0).

range from 55 to 75% cold reduction, is that the rearrangement of the elastic distortion for the crystal lattice and the new grain boundaries are formed by a large number of deformation reductions, resulting in the decrease in the degree of crystal lattice distortion.

The optical microstructures of the Ti–10Mo–6Zr–4Sn–3Nb alloy, cold swaged with different reductions corresponding to the axial direction, are shown in **Figure 2**. It can be seen that many slip bands interacting with adjacent grain boundaries are obviously observed in the β grains at different reductions. In **Figure 2A**, a few deformation bands gradually occur in some grains with the reduction of 15%. It can be inferred that the slip mode may elicit the appearance of deformation bands during cold deformation. As seen in **Figures 2B,C**, a small number of slip bands pass through the grain boundaries. The reason for this is the combination effect of the dislocation slip and the grain boundaries slip. In addition, **Figures 2D,E** show that the grains are obviously elongated along the axial direction with the ongoing reductions. The deformation mode of the experimental alloy changes from the dislocation slip and the elongation of the original grain boundaries, to the original grains crushing and transgranular shear bands deformation. When 65 and 75% cold swaging reductions are conducted, the grains appear to be distinctly distorted and elongated along the axial direction (in **Figures 2F,G**). It is noted that a combination of grain boundaries takes place. Moreover, it is difficult to distinguish the deformed grain boundary from the optical microstructure. It can be seen in **Figure 2H** that when the original β grains are subjected to severe deformation with a reduction of 75%, the swaged microstructure displays a typical "marble pattern." It has been reported that the formation of a microstructure with a "marble pattern" results from a large number of nanoscale lattice disturbances in the deformed metals and the development of many discontinuous stacking faults take place (Saito et al., 2003). The grains first form staggered layers along a certain crystal orientation. The region of extremely thin local lattice disturbance distributing along the staggered layers then plays a similar role in the grain boundary. The shear deformation is prevented in the direction of original stacking faults by forming new ones in the direction of other orientations.

Figure 3 presents the bright field (BF) images and the selected area diffraction (SAD) patterns for the samples that were cold swaged with various reductions. **Figure 3A** shows that the β matrix exhibits a typical light-dark structure. This structure may be a severe plastic deformed zone owing to the tangle and pile-up of dislocations around the grain boundaries. The corresponding SAD pattern indicates that there is only a single β phase in this region. **Figure 3B** shows the BF image and SAD pattern for the sample that was cold swaged with a reduction of 55%. The observed result is basically the same as the result observed at 25% reduction. The precipitates are also a lamellar α" martensite. However, the length of the α" martensite reduces, which may result from the grain refinement and, hence, inhibits the growth of the martensite phase. Additionally, the SAD pattern indicates that the orientation relationship between the α" and β phase follows $[1\ 1\ 0]_{\beta}$ //$[0\ 0\ 1]_{\alpha''}$. It can be concluded that the unit cell structure of the stress-induced α" martensite is about twice the size of the structure for the β phase. A certain habit plane would be maintained during the phase transformation from β to α", which is consistent with the result found by Ahmed et al. (2015). **Figure 3C** indicates that when the reduction increases to 75%, some α" martensite phases are still presented in the selection area, whereas no other deformation mechanism such as mechanical twins is found. Therefore, it can be inferred that the main mechanism of cold swaging deformation is considered to be stress-induced martensitic (SIM) transformation and dislocation slip. With the increment in the reduction during cold swaging, the deformation mode of the alloy remains.

In general, the formation of the martensite phase with an orthorhombic structure can be promoted by rapid cooling. In particular, the reason for SIM is mainly due to the driving force from the applied stress, which achieves the same effect as the thermodynamic process. The element diffusion among different phases is not induced in this period. Once the martensite phase grows to a definite size, this process is considered to be a lattice shear (Ma et al., 2019; Cho et al., 2020; Song et al., 2020). The appearance of SIM transformation has many influencing factors, including β stability, grain size, deformation temperature, and strain rate during the process (Sittner et al., 2018). Therefore, one can conclude that the high β stability of titanium alloys could lead to the reduction of martensite transformation temperature, resulting in the increment in the required applied stress.

The Influence of Swaging Deformation on Texture Evolution

The presentation of the pole figures (PF) and inverse pole figures (IPF) is one of the effective methods to illustrate the spatial orientation of crystals by means of two-dimensional figures. However, the PF and IPF are only stereographic projections of the grain orientation distribution on specific crystal planes; more crystallographic information cannot be completely reflected by this way. Bunge and Roe also proposed a three-dimensional (3D) ODFs for describing the polycrystal texture. The problem of expressing multidimensional orientation distribution uses a 3D orientation space (Wilkinson and Britton, 2012). According to Roe, the orientation of the crystal is determined using three Euler angles referring to (ψ, θ, φ). According to Bunge, (φ1, Φ, φ2) is used to illustrate the texture component based on the section of ODFs (Sneddon et al., 2016). For cubic crystal materials, the ODF cross-sectional diagrams of φ2 = 0° and φ2 = 45°can basically indicate the main texture components. In this work, for titanium alloys, the ODFs cross-sectional diagram of φ2 = 45° (**Figure 4A**) can show the swaged texture, including α-fiber ({0 0 1} <1 1 0>, {1 1 2} <1 1 0> and {1 1 1} <1 1 0>), and γ-fiber ({1 1 1} <1 1 2> and {1 1 1} <1 1 0>).

Figures 4A–D show the ODFs of samples after swaging deformation at φ2 = 45°. Overall, the samples deformed with the reductions of 15, 45, and 75% have a larger texture strength. In this work, it can be seen that in the case of a low reduction (15%), α-fiber {1 1 2} <1 1 0>, {1 1 2} < 1 1 1 > , γ-fiber {1 1 1} <1 1 2> texture, and a strong texture of {1 1 0} <1 1 2> are presented (**Figure 4B**). When the reduction is moderate (45%), the textures

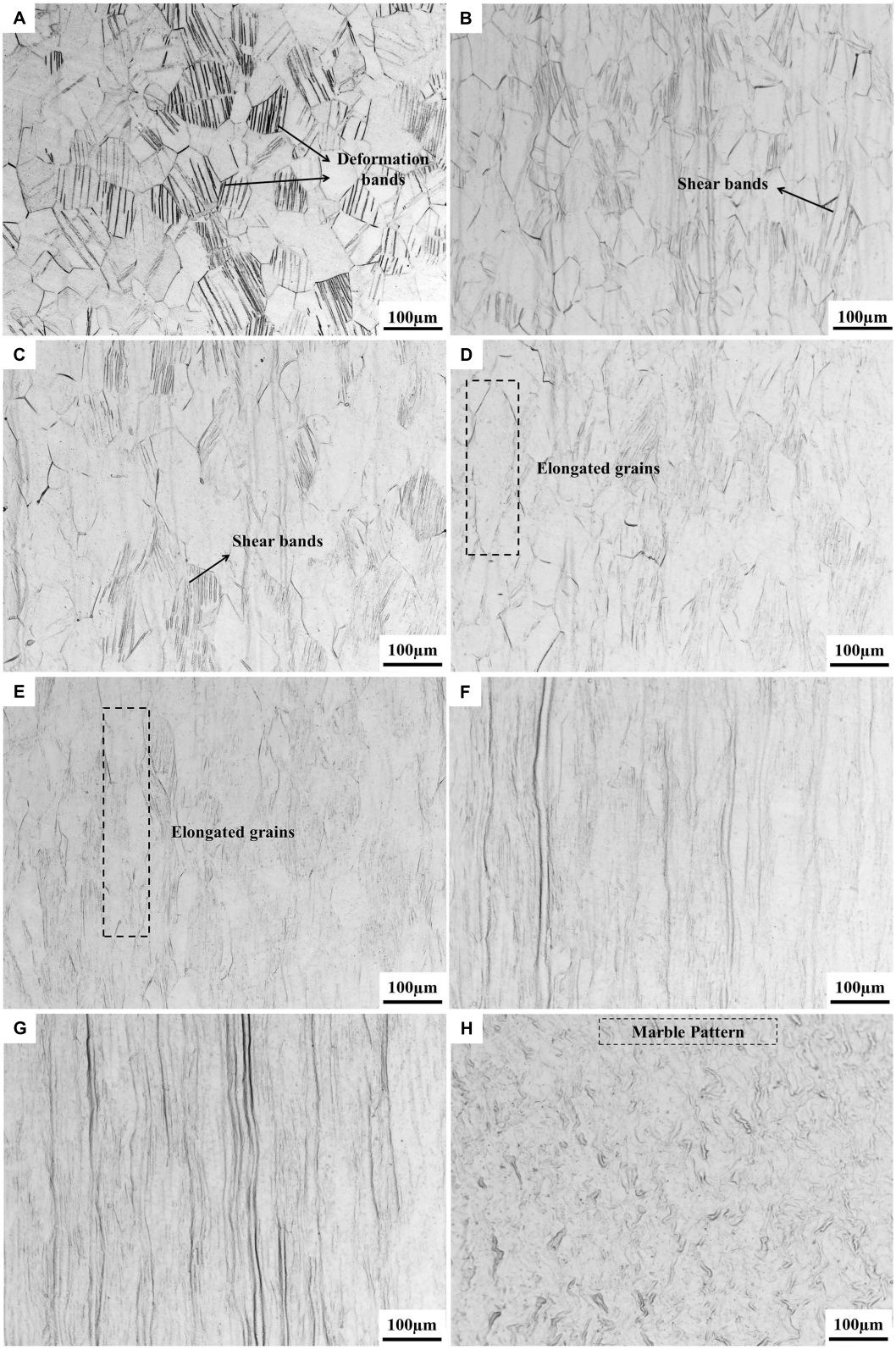

FIGURE 2 | Optical microstructures of the Ti–10Mo–6Zr–4Sn–3Nb alloy cold swaged with reductions of: **(A)** 15%, **(B)** 25%, **(C)** 35%, **(D)** 45%, **(E)** 55%, **(F)** 65%, and **(G,H)** 75%. The samples of **(A–G)** were taken from the longitudinal section of the alloy bars; The sample of **(H)** was cut from the cross section of the experimental alloy bar.

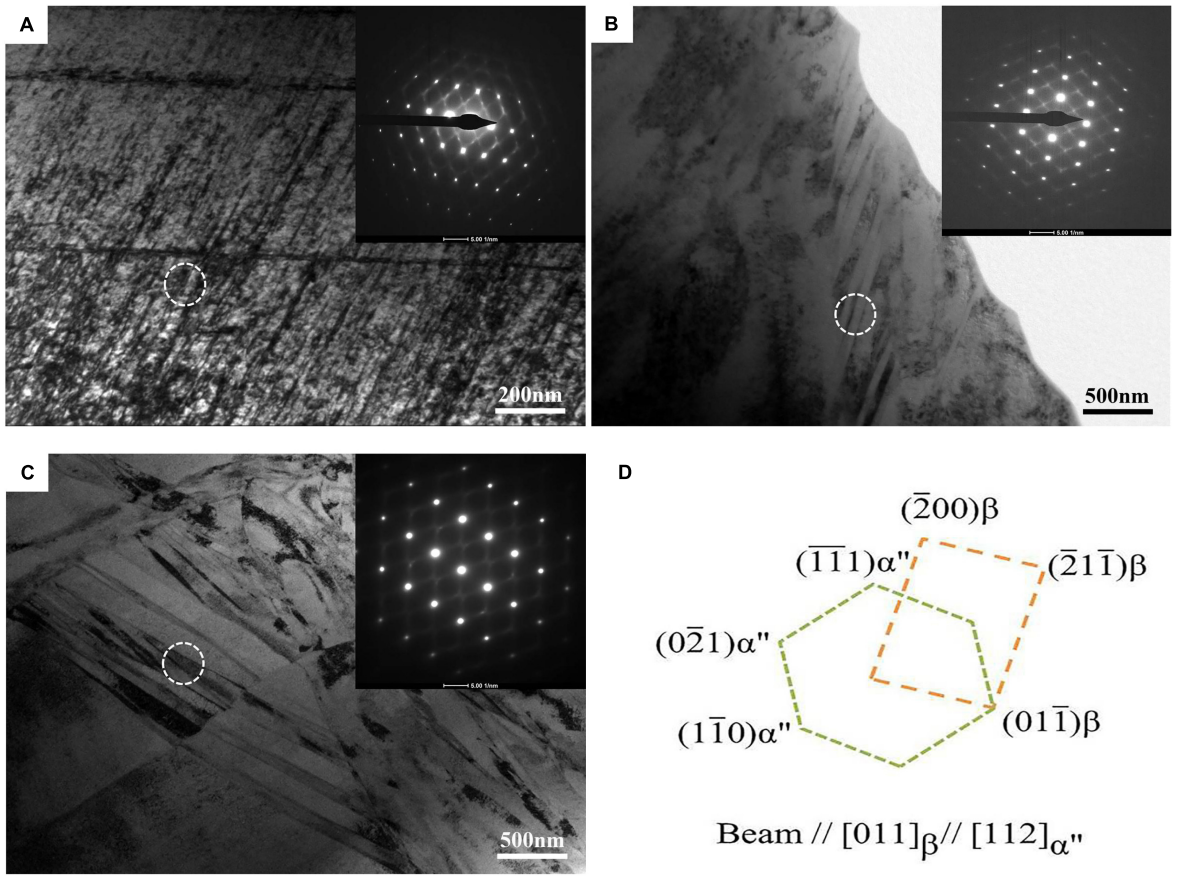

FIGURE 3 | TEM BF images and SAD patterns of the Ti–10Mo–6Zr–4Sn–3Nb alloy cold swaged with reductions of: **(A)** 25%, **(B)** 55%, and **(C)** 75%, **(D)** Schematic diagram of the Burgers relationship between stress-induced martensite and the β matrix (BF: Bright Field; SAD: Selected Area Diffraction).

of {1 1 2} <1 1 1>, {1 1 1} <1 1 2>, and {1 1 0} <1 1 2> disappear, and the weak α-fiber {1 1 2} <1 1 0> is still presented (**Figure 4C**). Moreover, the newly generated γ-fiber {1 1 1} <1 1 0> is stronger than the others. Furthermore, for a high reduction (75%), the texture component is, overall, unchanged (**Figure 4D**). The α-fiber {1 1 2} <1 1 0> is strengthened, and the strength of the γ-fiber {1 1 1} <1 1 0> is also improved. It is clearly indicated that the grain orientation appears to be rotated along the axis of <1 1 0>.

From the above sections, it can clearly be found that the textures of {1 1 0} <1 1 2> and {1 1 1} <1 1 2> gradually weaken and finally disappear during the cold swaging deformation. Recent studies (Xu et al., 2012) showed that the dynamic recrystallization results in the formation of {1 1 0} <1 1 2> and {1 1 1} <1 1 2> textures after hot rolling with a 71% reduction and solution annealing at 900°C/1 h. Sander and Raabe (2008) investigated the texture inhomogeneity of the Ti–35Nb–7Zr–5Ta alloy after thermal deformation followed by solution annealing; they found that an obvious {1 1 1} <1 1 2> texture component exists in the samples. γ-fiber {1 1 1} <1 1 0> gradually increased when increasing the reduction. Inamura et al. (2005) found that the {0 0 1} <1 1 0> corresponding to the γ-type texture was dominant in the Ti–Al–Nb based titanium alloy cold deformed with a 99% reduction. The reason, accounting for the intensity of the α-fiber {1 1 2} <1 1 0> texture showing first a decrease and then an increase trend when increasing the reduction, is still not completely understood. However, the intensity of the α-fiber texture is enhanced at a larger reduction and has been reported in several various β Ti alloys. Lan et al. (2017) investigated the texture evolution of a cold-rolled TNZS (Ti–32.5Nb–6.8Zr–2.7Sn) alloy and found that the {0 0 1} <1 1 0> texture is presented again when the reduction of cold rolling is 90%. Therefore, in this work, the texture evolution of the Ti–10Mo–6Zr–4Sn–3Nb alloy results from the relatively high crystallographic stability of the <1 1 0> preferred orientation during the low and intermediate plane strain deformation. Furthermore, the texture is also influenced by the processing history of the alloy itself.

The Influence of Swaging Deformation on Mechanical Properties

Figure 5 presents the mechanical properties for the metastable β type Ti–10Mo–6Zr–4Sn–3Nb alloy after solution treatment plus cold swaging deformation at room temperature. It is evident from **Figure 5A** that the tensile strength increases with

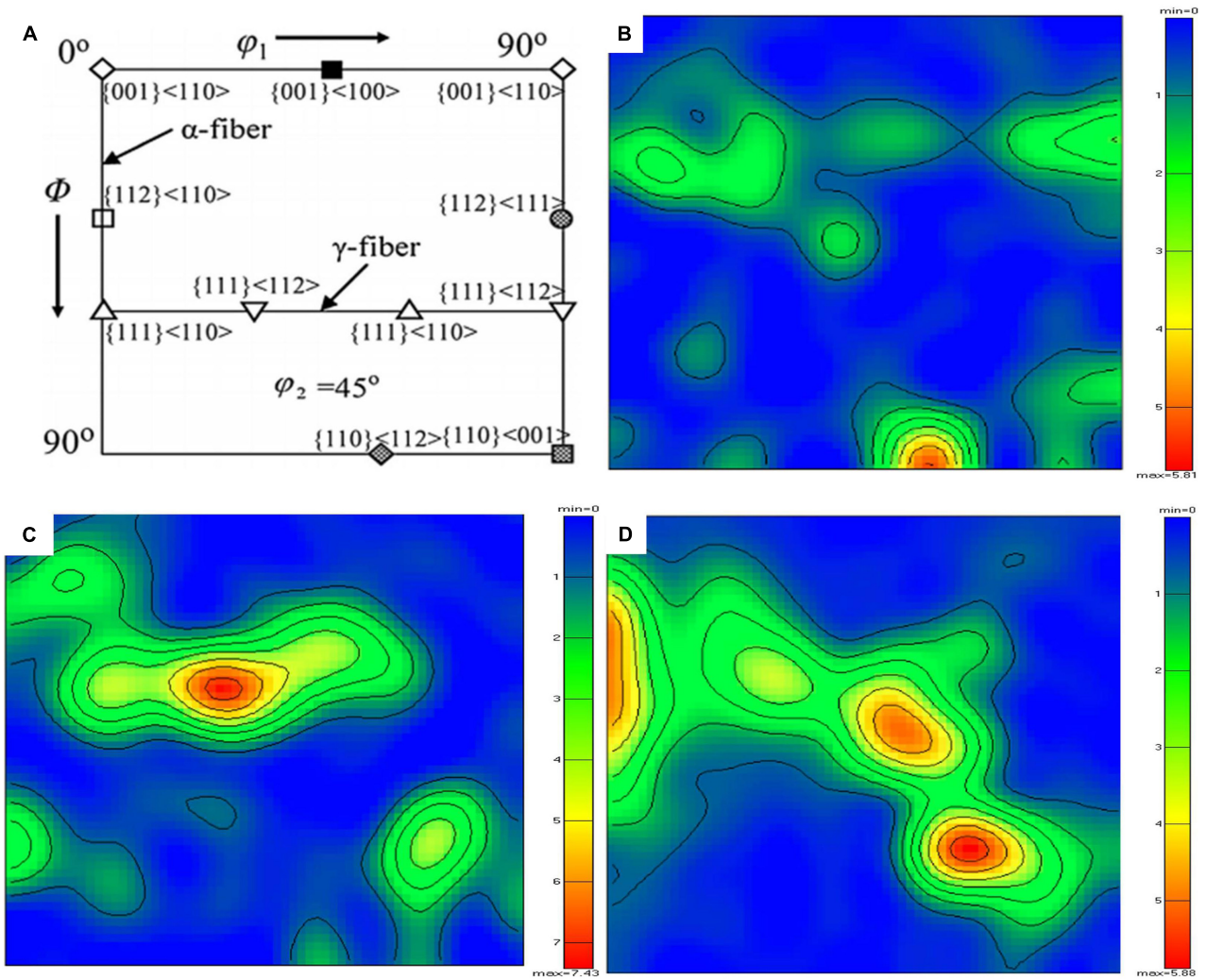

FIGURE 4 | Sections (φ2 = 45°) of the orientation distribution functions (ODFs) on the rolling plane for the β phase of the Ti–10Mo–6Zr–4Sn–3Nb alloy: **(A)** schematic diagram of section (φ2 = 45°) of the ODFs with typical texture components corresponding to the body-centered cubic metallic materials; cold swaging deformed at **(B)** 25%, **(C)** 55%, and **(D)** 75%.

an increase in the reduction of swaging deformation. When the reduction reaches 75%, the tensile strength (1324 MPa) is higher than the counterpart after solution treatment (932 MPa). The strengthening effect caused by accumulative swaging deformation is very pronounced, and the total increment is about 42.1% compared with the original. The reasons for the obvious increase in strength are mainly due to the following three factors: (1) The grain size is refined after cold swaging deformation. The enhancement of strength can be explained by the Hall-Petch's law. (2) There is a large number of sub-structures, dislocation tangles, and pile-ups, resulting in the formation of sub-grains (Conrad, 1981). (3) The <1 1 0> texture intensity of the Ti–10Mo–6Zr–4Sn–3Nb alloy gradually increases when increasing the reduction during cold deformation, leading to the effect of texture strengthening (Zhang et al., 2011).

The relationship between reduction, Young's modulus (E), and the reduction of the area is shown in **Figure 5B**. It can be found that the reduction of the area of the cold swaging deformed specimen is lower than that of the solution-treated one. The reduction of the area is always maintained over 40% when increasing the reduction, showing excellent plasticity at room temperature. In addition, the Young's moduli of the samples mainly display a decreasing tendency with the increase in the reduction. The reasons for the decrease in the Young's modulus are as follows: first, the elastic modulus is associated with the lattice constants and interatomic distance for β type titanium alloys. According to the previous studies (Matsumoto et al., 2007; Tane et al., 2008; Liu et al., 2014; Liu et al., 2015), the Young's modulus of the α" martensite phase is lower than that of the β phase in several β Ti alloys. The increment in the shear modulus is caused by the formation of the ω phase transformation from the α phase during low temperature aging, resulting in an increase in the modulus for a newly developed β type Ti–25Nb–10Ta–5Zr alloy. Similar

results were obtained in this work. It was found that the transformation of β→α" is induced in the Ti–10Mo–6Zr–4Sn–3Nb alloy after cold swaging. Moreover, the cold swaging plastic deformation would promote the grain refinement and the increment in sub-grains and sub-boundaries. The distances between the atoms at the grain boundaries might be longer than those inside the grains, resulting in a decrease in the modulus. Second, the decrease in the modulus results from the formation of a huge number of dislocations during the cold swaging deformation. The effect of dislocations on the Young's modulus was first proposed by Mott et al. (1975); when the metallic material is subjected to the external stress, the dislocation lines under the pinning effect of the solute atoms would be bended, resulting in an additional elastic deformation and the decrease in the Young's modulus. The change in the Young's modulus (E) can be expressed by the following equation:

$$\frac{\Delta E}{E} = -\rho\frac{l^2}{6a} \quad (1)$$

Where ρ is the density of dislocations, l is the average length of dislocations between the pinning points, and α is a function of the average length of dislocations. The effect of a decrease in the elastic modulus caused by this type of cold deformation mechanism was systematically studied in copper and iron alloys (Ledbetter and Kim, 1988; Benito et al., 2005). In addition, the elastic modulus of the β phase has an anisotropic feature during plastic deformation at various reductions. Gutkin et al. (2008)

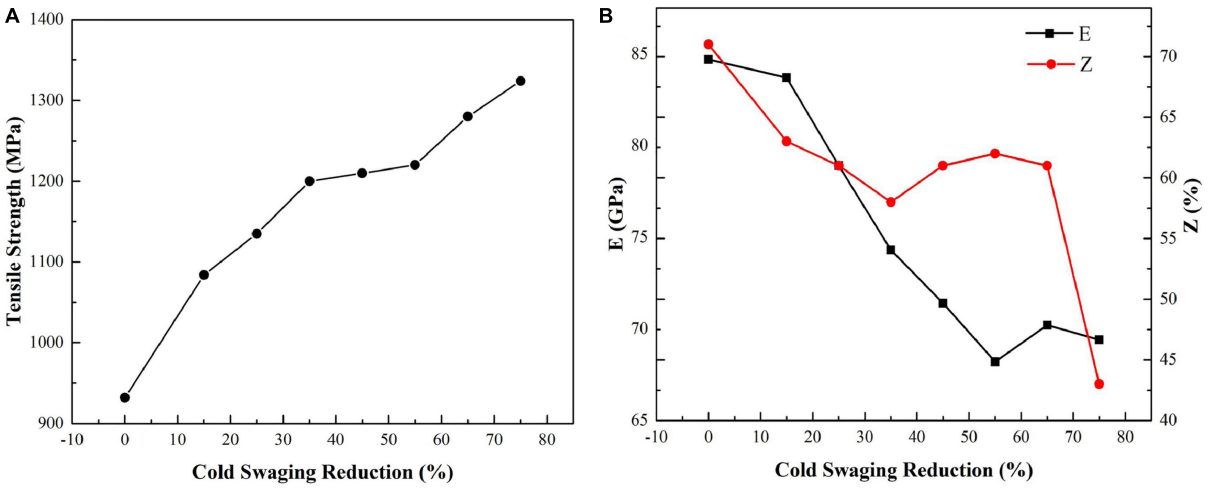

FIGURE 5 | Relationship between cold swaging reduction and mechanical properties of solution-treated and swaging deformed specimens, taken from the longitudinal direction: **(A)** tensile strength and **(B)** elastic modulus, and reduction of area.

TABLE 2 | Mechanical properties of the Ti–10Mo–6Zr–4Sn–3Nb alloy and some typical metallic materials used for biomedical applications.

Alloys	Phase composition	Tensile strength (MPa)	Elongation (%)	Elastic modulus (GPa)	Ratio of strength-to-elastic modulus/ × 10^{-3}	References
ST Ti–10Mo–6Zr–4Sn–3Nb	β	932	23.5	84.7	11.0	Present work
CS 15% Ti–10Mo–6Zr–4Sn–3Nb	β + α"	1084	15.0	83.7	12.9	Present work
CS 25% Ti–10Mo–6Zr–4Sn–3Nb	β + α"	1135	15.0	78.9	14.4	Present work
CS 35% Ti–10Mo–6Zr–4Sn–3Nb	β + α"	1200	12.0	74.3	16.2	Present work
CS 45% Ti–10Mo–6Zr–4Sn–3Nb	β + α"	1210	14.5	71.4	16.9	Present work
CS 55% Ti–10Mo–6Zr–4Sn–3Nb	β + α"	1220	11.5	68.2	17.8	Present work
CS 65% Ti–10Mo–6Zr–4Sn–3Nb	β + α"	1280	10.5	70.2	18.2	Present work
CS 75% Ti–10Mo–6Zr–4Sn–3Nb	β + α"	1324	5.5	69.4	18.9	Present work
CP Ti	α	240–550	15–24	103–104	2.3–5.3	Niinomi, 1998
Ti–6Al–4V	α + β	895–930	6–10	110–114	7.9–8.5	Niinomi, 1998
Ti–6Al–7Nb	α + β	900–1050	8.1–15	114	7.9–9.2	Niinomi, 1998
Ti–29Nb–13Ta–4.6Zr	β	911	13.2	80	11.4	Niinomi, 1998
ASTM F75 (Co–Cr–Mo based alloy)		600–1795	–	200–230	2.6–9.0	Long and Rack, 1998
316L	–	465–950	–	200	2.3–4.8	Long and Rack, 1998

ST, solution treatment; CS: cold swaging.

found that the Young's modulus of metals with a BCC structure, in given orientations corresponding to polycrystal, can be calculated using the elastic constants c_{11}, c_{12}, and c_{44} in the following equation:

$$E = (c_{11} - c_{12} + 3c_{44})(c_{11} + 2c_{12})/(2c_{11} + 3c_{12} + c_{44}) \quad (2)$$

The elastic modulus of the β phase is anisotropic. The minimum value of the elastic modulus for the β phase is obtained in the [0 0 1] orientation and gradually increases in the order of [0 0 1] < [110] < [1 1 1]∼[1 1 2] (Kim et al., 2006; Masumoto et al., 2006). It is evident from the above results that the textures of <1 1 2> and <1 1 1> gradually weaken and finally disappear after cold swaging deformation. By contrast, the texture of <1 1 0> is strengthened due to the rotation of individual grains after a certain reduction of the sample, leading to the reduction of the modulus.

Table 2 presents a summary of the mechanical properties of the Ti–10Mo–6Zr–4Sn–3Nb alloy and some typical biomedical metallic materials. For orthopedic applications, elastic allowable strain is an important parameter, defined as the ratio of tensile strength (UTS) to the elastic modulus (*E*). In general, the alloy with a higher ratio of a strength-to-elastic modulus indicates that it possesses better comprehensive mechanical properties. The ratio of the strength-to-elastic modulus of the experimental alloy after cold swaging, gradually increases. It can be found that the maximum value of the ratio is 18.9×10^{-3}. Compared with other common metallic implant biomaterials, including 316L, commercially pure titanium, Ti6Al4V, Ti6Al7Nb, and another newly developed β Ti–29Nb–13Ta–4.6Zr alloy, the Ti–10Mo–6Zr–4Sn–3Nb alloy is considered to possess greater advantages for the future (Long and Rack, 1998; Niinomi, 1998). From the perspective of surgical implant development, the titanium alloy with a higher strength, acceptable elongation, low Young's modulus and non-toxic elements is considered to have very high potential in the application for orthopedics. When the Ti–10Mo–6Zr–4Sn–3Nb alloy is subjected to cold swaging with a reduction of 65%, the tensile strength is 1280 MPa, the elastic modulus is 70.2 GPa, and the elongation is 10.5%, which can be considered as having attractive comprehensive properties.

CONCLUSION

The effect of cold swaging deformations on the microstructure characteristic, texture evolution, and mechanical properties for a metastable β Ti–10Mo–6Zr–4Sn–3Nb titanium alloy for biomedical devices was investigated. The main conclusions are as follows:

(1) With the increase in cold swaging reduction, stress-induced martensite (SIM) transformation takes place, leading to the formation of the α" phase.
(2) The dislocation sub-structures, deformation bands, as well as rotation and elongation of grains along the axial direction are generated in the deformed microstructures of the Ti–10Mo–6Zr–4Sn–3Nb alloy. Moreover, the deformed grains are broken and refined step by step during cold swaging deformation at various reductions.
(3) The {1 1 2} <1 1 1> and {1 1 0} <1 1 2> textures transform into γ-fiber {1 1 1} <1 1 0> and α-fiber {1 1 2} <1 1 0> with an increment in the reduction of cold swaging. The α-fiber texture first weakens and then strengthens during cold swaging at various reductions.
(4) The Ti–10Mo–6Zr–4Sn–3Nb alloy solution treated in the β phase region (790°C/1 h, WQ) shows outstanding cold workability during swaging deformation. The ductility maintains at a moderate level due to the original grains which have not been fully broken at the commencement of the cold swaging.
(5) The elastic modulus of the Ti–10Mo–6Zr–4Sn–3Nb alloy exhibits a downward tendency with the increment in reduction, which is associated with dislocation multiplication, grain refinement, and grain orientation evolution during cold swaging, with reductions of 15% to 75%.

DATA AVAILABILITY STATEMENT

All datasets presented in this study are included in the article/**Supplementary Material**.

AUTHOR CONTRIBUTIONS

JC took charge of the original draft writing. HW took charge of the data analysis and literature investigation. JL took charge of the technical guidance and supervision. JG and HS took charge of the preparation of specimens. JR took charge of the cold swaging. ZD took charge of the microstructure characterization. JF took charge of the mechanical properties testing. JN and ZY took charge of the technical reviewing. All authors contributed to the article and approved the submitted version.

FUNDING

This study was supported by the State Key Laboratory of Powder Metallurgy, Central South University, Changsha, China (621011823); the Key Research and Development Program of Shaanxi (Program Nos. 2019GY-151, 2019GY-178, 2020GY-251); the National Natural Science Foundation of China (51901193, 51861029); the Science and Technology Plan Project of Weiyang District in Xi'an City (201905); and the Science and Technology Project of Xi'an (2020KJRC0141).

REFERENCES

Ahmed, M., Wexler, D., Casillas, G., Ivasishin, O. M., and Pereloma, E. V. (2015). The influence of β phase stability on deformation mode and compressive mechanical properties of Ti-10V-3Fe-3Al alloy. *Acta Mater.* 84, 124–135. doi: 10.1016/j.actamat.2014.10.043

Bahl, S., Das, S., Suwas, S., and Chatterjee, K. (2018). Engineering the next-generation tin containing β titanium alloys with high strength and low modulus for orthopedic applications. *J. Mech. Behav. Biomed. Mater.* 78, 124–133. doi: 10.1016/j.jmbbm.2017.11.014

Banerjee, D., and Williams, J. C. (2013). Perspectives on titanium science and technology. *Acta Mater.* 61, 844–879. doi: 10.1016/j.actamat.2012.10.043

Benito, J. A., Jorba, J., Manero, J. M., and Roca, A. (2005). Change of Young's modulus of cold-deformed pure iron in a tensile test. *Metallurgical Mater. Trans. A Phys. Metallurgy Mater. Sci.* 36, 3317–3324. doi: 10.1007/s11661-005-0006-6

Cai, S., Daymond, M. R., Ren, Y., Bailey, D. M., and Kay, L. E. (2013). Influence of short time anneal on recoverable strain of beta III titanium alloy. *Mater. Sci. Eng. A Struct. Mater. Properties Microstruct. Process.* 562, 172–179. doi: 10.1016/j.msea.2012.11.005

Callioglu, Ş, and Acar, P. (2020). Design of β-Titanium microstructures for implant materials. *Mater. Sci. Eng. C* 110:110715. doi: 10.1016/j.msec.2020.110715

Chen, Q., and Thouas, G. A. (2015). Metallic implant biomaterials. *Mater. Sci. Eng. R-Rep.* 87, 1–57. doi: 10.1016/j.mser.2014.10.001

Cho, K., Morioka, R., Harjo, S., Kawasaki, T., and Yasuda, H. Y. (2020). Study on formation mechanism of {332}(113(deformation twinning in metastable β-type Ti alloy focusing on stress-induced α" martensite phase. *Scripta Mater.* 177, 106–111. doi: 10.1016/j.scriptamat.2019.10.011

Conrad, H. (1981). Effect of interstitial solutes on the strength and ductility of titanium. *Progr. Mater. Sci.* 26, 123–403. doi: 10.1016/0079-6425(81)90001-3

Eisenbarth, E., Velten, D., Muller, M., Thull, R., and Breme, J. (2004). Biocompatibility of β-stabilizing elements of titanium alloys. *Biomaterials* 25, 5705–5713. doi: 10.1016/j.biomaterials.2004.01.021

Geetha, M., Singh, A. K., Asokamani, R., and Gogia, A. K. (2009). Ti based biomaterials, the ultimate choice for orthopaedic implants – A review. *Progr. Mater. Sci.* 54, 397–425. doi: 10.1016/j.pmatsci.2008.06.004

Gepreel, M. A., and Niinomi, M. (2013). Biocompatibility of Ti-alloys for long-term implantation. *J. Mech. Behav. Biomed. Mater.* 20, 407–415. doi: 10.1016/j.jmbbm.2012.11.014

Gutkin, M. Y., Ishizaki, T., Kuramoto, S., Ovidko, I. A., and Skiba, N. V. (2008). Giant faults in deformed Gum Metal. *Int. J. Plasticity* 24, 1333–1359. doi: 10.1016/j.ijplas.2007.09.009

Hao, Y., Li, S., Sun, B., Sui, M. L., and Yang, R. (2007). Ductile titanium alloy with low poisson's ratio. *Phys. Rev. Lett.* 98:216405.

Hao, Y., Zhang, Z., Li, S., and Yang, R. (2012). Microstructure and mechanical behavior of a Ti-24Nb-4Zr-8Sn alloy processed by warm swaging and warm rolling. *Acta Mater.* 60, 2169–2177. doi: 10.1016/j.actamat.2012.01.003

Ibrahim, M. Z., Sarhan, A. A. D., Yusuf, F., and Hamdi, M. (2017). Biomedical materials and techniques to improve the tribological, mechanical and biomedical properties of orthopedic implants – A review article. *J. Alloys Compounds* 714, 636–667. doi: 10.1016/j.jallcom.2017.04.231

Inamura, T., Fukui, Y., Hosoda, H., Wakashima, K., and Miyazaki, S. (2005). Pseudoelastic properties of cold-rolled TiNbAl alloy. *Mater. Sci. Forum* 475–479, 2323–2328. doi: 10.4028/www.scientific.net/msf.475-479.2323

Kim, H. Y., Ikehara, Y., Kim, J. I., Hosoda, H., and Miyazaki, S. (2006). Martensitic transformation, shape memory effect and superelasticity of Ti-Nb binary alloys. *Acta Mater.* 54, 2419–2429. doi: 10.1016/j.actamat.2006.01.019

Lan, C., Wu, Y., Guo, L., Chen, H., and Chen, F. (2017). Microstructure, texture evolution and mechanical properties of cold rolled Ti-32.5Nb-6.8Zr-2.7Sn biomedical beta titanium alloy. *J. Mater. Sci. Technol.* 34, 788–792. doi: 10.1016/j.jmst.2017.04.017

Ledbetter, H., and Kim, S. (1988). Molybdenum effect on Fe–Cr–Ni-alloy elastic constants. *J. Mater. Res.* 3, 40–44. doi: 10.1557/jmr.1988.0040

Li, H. F., and Zheng, Y. (2016). Recent advances in bulk metallic glasses for biomedical applications. *Acta Biomater.* 36, 1–20. doi: 10.1016/j.actbio.2016.03.047

Li, X., Ye, S., Yuan, X., and Yu, P. (2019). Fabrication of biomedical Ti-24Nb-4Zr-8Sn alloy with high strength and low elastic modulus by powder metallurgy. *J. Alloys Compounds* 772, 968–977. doi: 10.1016/j.jallcom.2018.08.262

Liang, Q., Kloenne, Z., Zheng, Y., Wang, D., Antonov, S., Gao, Y., et al. (2020). The role of nano-scaled structural non-uniformities on deformation twinning and stress-induced transformation in a cold rolled multifunctional β-titanium alloy. *Scripta Mater.* 177, 181–185. doi: 10.1016/j.scriptamat.2019.10.029

Liu, H., Niinomi, M., Nakai, M., and Cho, K. (2015). β-Type titanium alloys for spinal fixation surgery with high Young's modulus variability and good mechanical properties. *Acta Biomater.* 24, 361–369. doi: 10.1016/j.actbio.2015.06.022

Liu, H., Niinomi, M., Nakai, M., Hieda, J., and Cho, K. (2014). Changeable Young's modulus with large elongation-to-failure in β-type titanium alloys for spinal fixation applications. *Scripta Mater.* 82, 29–32. doi: 10.1016/j.scriptamat.2014.03.014

Long, M., and Rack, H. J. (1998). Titanium alloys in total joint replacement—a materials science perspective. *Biomaterials* 19, 1621–1639. doi: 10.1016/s0142-9612(97)00146-4

Ma, X., Li, F., Fang, X., Li, Z., Sun, Z., Hou, J., et al. (2019). Effect of strain reversal on the stress-induced martensitic transformation and tensile properties of a metastable β titanium alloy. *J. Alloys Compounds* 784, 111–116. doi: 10.1016/j.jallcom.2019.01.010

Masumoto, K., Horiuchi, Y., Inamura, T., Hosoda, H., Wakashima, K., Kim, H. Y., et al. (2006). Effects of Si addition on superelastic properties of Ti–Nb–Al biomedical shape memory alloys. *Mater. Sci. Eng. A-Struct. Mater. Properties Microstruct. Process.* 438, 835–838. doi: 10.1016/j.msea.2006.02.060

Matsumoto, H., Watanabe, S., and Hanada, S. (2007). Microstructures and mechanical properties of metastable β TiNbSn alloys cold rolled and heat treated. *J. Alloys Compounds* 439, 146–155. doi: 10.1016/j.jallcom.2006.08.267

Meng, Q., Guo, S., Liu, Q., Hu, L., and Zhao, X. (2014). A β-type TiNbZr alloy with low modulus and high strength for biomedical applications. *Progr. Nat. Sci.* 24, 157–162. doi: 10.1016/j.pnsc.2014.03.007

Mori, M., Sato, N., Yamanaka, K., Yoshida, K., Kuramoto, K., and Chiba, A. (2016). Development of microstructure and mechanical properties during annealing of a cold-swaged Co–Cr–Mo alloy rod. *J. Mech. Behav. Biomed. Mater.* 64, 187–198. doi: 10.1016/j.jmbbm.2016.07.009

Mott, N. F., Davis, E. A., and Street, R. A. (1975). States in the gap and recombination in amorphous semiconductors. *Philos. Magazine* 32, 961–996. doi: 10.1080/14786437508221667

Niinomi, M. (1998). Mechanical properties of biomedical titanium alloys. *Mater. Sci. Eng. A-Struct. Mater. Properties Microstruct. Process.* 243, 231–236. doi: 10.1016/s0921-5093(97)00806-x

Niinomi, M. (2008). Mechanical biocompatibilities of titanium alloys for biomedical applications. *J. Mech. Behav. Biomed. Mater.* 1, 30–42. doi: 10.1016/j.jmbbm.2007.07.001

Niinomi, M., Nakai, M., and Hieda, J. (2012). Development of new metallic alloys for biomedical applications. *Acta Biomater.* 8, 3888–3903. doi: 10.1016/j.actbio.2012.06.037

Plaine, A. H., Silva, M. R. D., and Bolfarini, C. (2019). Microstructure and elastic deformation behavior of β-type Ti-29Nb-13Ta-4.6Zr with promising mechanical properties for stent applications. *J. Mater. Res. Technol.* 8, 3852–3858. doi: 10.1016/j.jmrt.2019.06.047

Qi, L., Qiao, X., Huang, L., Huang, X., Xiao, W., and Zhao, X. (2019). Effect of cold rolling deformation on the microstructure and properties of Ti-10V-2Fe-3Al alloy. *Mater. Characterization* 155:109789. doi: 10.1016/j.matchar.2019.109789

Rabadia, C. D., Liu, Y., Chen, L. Y., Jawed, S. F., and Zhang, L. C. (2019a). Deformation and strength characteristics of laves phases in titanium alloys. *Mater. Design* 179:107891. doi: 10.1016/j.matdes.2019.107891

Rabadia, C. D., Liu, Y. J., Zhao, C. H., Wang, J. C., and Zhang, L. C. (2019b). Improved trade-off between strength and plasticity in titanium based metastable beta type Ti-Zr-Fe-Sn alloys. *Mater. Sci. Eng. A* 766:138340. doi: 10.1016/j.msea.2019.138340

Ramezannejad, A., Xu, W., Xiao, W. L., Fox, K., Liang, D., and Qian, M. (2019). New insights into nickel-free superelastic titanium alloys for biomedical applications. *Curr. Opin. Solid State Mater. Sci.* 23:100783. doi: 10.1016/j.cossms.2019.100783

Saito, T., Furuta, T., Hwang, J., Kuramoto, S., Nishino, K., Suzuki, N., et al. (2003). Multifunctional alloys obtained via a dislocation-free plastic deformation mechanism. *Science* 300, 464–467. doi: 10.1126/science.1081957

Sander, B., and Raabe, D. (2008). Texture inhomogeneity in a Ti–Nb-based β-titanium alloy after warm rolling and recrystallization. *Mater. Sci. Eng. A-Structural Mater. Properties Microstruct. Process.* 479, 236–247. doi: 10.1016/j.msea.2007.06.077

Sittner, P., Sedlak, P., Seiner, H., Sedmak, P., Pilch, J., Delville, R., et al. (2018). On the coupling between martensitic transformation and plasticity in NiTi: Experiments and continuum based modelling. *Progr. Mater. Sci.* 98, 249–298. doi: 10.1016/j.pmatsci.2018.07.003

Sneddon, G., Trimby, P., and Cairney, J. M. (2016). Transmission Kikuchi diffraction in a scanning electron microscope: a review. *Mater. Sci. Eng. R-Rep.* 110, 1–12. doi: 10.1016/j.mser.2016.10.001

Song, X., Xiong, C., Zhang, F., Nie, Y., and Li, Y. (2020). Strain induced martensite stabilization in β Ti-Zr-Nb shape memory alloy. *Mater. Lett.* 259:126914. doi: 10.1016/j.matlet.2019.126914

Tane, M., Akita, S., Nakano, T., Hagihara, K., Umakoshi, Y., Niinomi, M., et al. (2008). Peculiar elastic behavior of Ti–Nb–Ta–Zr single crystals. *Acta Mater.* 56, 2856–2863. doi: 10.1016/j.actamat.2008.02.017

Wang, L., Lu, W., Qin, J., Zhang, F., and Zhang, D. (2008). Microstructure and mechanical properties of cold-rolled TiNbTaZr biomedical β titanium alloy. *Mater. Sci. Eng. A-Struct. Mater. Properties Microstruct. Process.* 490, 421–426.

Wilkinson, A. J., and Britton, T. B. (2012). Strains, planes, and EBSD in materials science. *Mater. Today* 15, 366–376. doi: 10.1016/s1369-7021(12)70163-3

Xu, T., Li, J. S., Zhang, S., Zhang, F., and Liu, X. (2016). Cold deformation behavior of the Ti-15Mo-3Al-2.7Nb-0.2Si alloy and its effect on α precipitation and tensile properties in aging treatment. *J. Alloys Compounds* 682, 404–411. doi: 10.1016/j.jallcom.2016.04.293

Xu, Y., Yi, D., Liu, H., Wu, X., Wang, B., and Yang, F. L. (2012). Effects of cold deformation on microstructure, texture evolution and mechanical properties of Ti–Nb–Ta–Zr–Fe alloy for biomedical applications. *Mater. Sci. Eng. A-Struct. Mater. Properties Microstruct. Process.* 547, 64–71. doi: 10.1016/j.msea.2012.03.081

Zhan, H., Wang, G., Kent, D., and Dargusch, M. S. (2016). The dynamic response of a metastable β Ti–Nb alloy to high strain rates at room and elevated temperatures. *Acta Mater.* 105, 104–113. doi: 10.1016/j.actamat.2015.11.056

Zhang, L. C., and Chen, L. Y. (2019). A review on biomedical titanium alloys: recent progress and prospect. *Adv. Eng. Mater.* 21:1801215. doi: 10.1002/adem.201801215

Zhang, L. C., Chen, L. Y., and Wang, L. Q. (2020). Surface modification of titanium and titanium alloys: technologies, developments, and future interests. *Adv. Eng.Mater.* 22:1901258. doi: 10.1002/adem.201901258

Zhang, M., Li, Y. N., Zhang, F. C., Wang, X. B., Chen, L. Y., and Yang, Z. N. (2017). Effect of annealing treatment on the microstructure and mechanical properties of a duplex Zr-2.5Nb alloy. *Mater. Sci. Eng. A* 706, 236–241. doi: 10.1016/j.msea.2017.08.107

Zhang, Y., Li, S., Obbard, E. G., Wang, H., Wang, S., Hao, Y., et al. (2011). Elastic properties of Ti-24Nb-4Zr-8Sn single crystals with bcc crystal structure. *Acta Mater.* 59, 3081–3090. doi: 10.1016/j.actamat.2011.01.048

Conflict of Interest: The authors declare that the research was conducted in the absence of any commercial or financial relationships that could be construed as a potential conflict of interest.